Detecting Human Posterior Lens Surface Topographical Changes During Accommodation

E. Feldman[1], Y. Chen[2], R. Schachar[3] and P. Cosman[2]

1. Milken Community Schools, Los Angeles, California, USA
2. Department of Electrical and Computer Engineering, UC San Diego, San Diego, California, USA
3. Department of Physics, University of Texas at Arlington, Arlington Texas, USA

efeldman646@milkenschool.org, yic041@eng.ucsd.edu, ron@2ras.com, pcosman@eng.ucsd.edu

Accommodation is the eye's ability to focus up close by changing the shape of the lens. Accommodation affects the development of myopia and glaucoma and its age-related decline results in presbyopia. Presbyopia affects 100% of the population in the fifth decade of life. An understanding of accommodation is required to develop the best treatments for these maladies, but how the lens changes shape is still in dispute after more than 165 years. The fundamental issue is whether the change in lens shape results from all zonules (circumferential suspensory ligaments that connect the lens of the eye to the ciliary body) relaxing, which causes central and peripheral lens surface steepening, or whether instead just the anterior and posterior zonules relax while the equatorial zonules are under increased tension, which causes the lens surface to peripherally flatten and centrally steepen. The alternatives are illustrated in Figure 1.

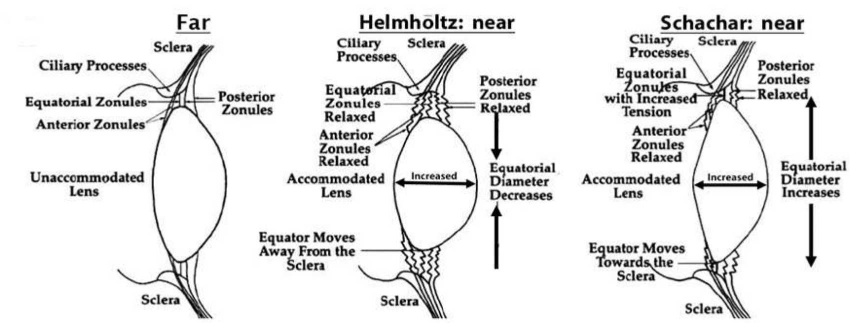

Figure 1. Schematic of theories of accommodation (focusing up close) according to Helmholtz [1] and Schachar [2]

Although profiles of the lens anterior and posterior surfaces can be obtained by magnetic resonance imaging (MRI), Schiempflug photography, and optical coherence tomography (OCT), curve fitting is required with these approaches. Fitting reduces the detection accuracy of small changes of the peripheral lens surfaces, whose characterization is critical to understanding the accommodation mechanism. The advantage of using the reflection-based approach proposed in this paper is that small changes are magnified; however, the reflections are very dim, requiring state of the art equipment and algorithms for detection.

Placido disc topography is routinely used for keratometry (measuring corneal curvature). In a novel optical setup, we instead use the reflection of the semi-circular rings from the inferior posterior lens surface (P_{IV}SRs) of the lower half of an illuminated Placido disc (with 24 equally spaced rings, 12 illuminated and 12 black) to assess topographical posterior lens surface changes during *in vivo* human accommodation. Video-graphic images of P_{IV}SRs were obtained from a 20-year-old male subject who in both eyes had a normal ophthalmic examination, uncorrected visual acuity of 20/20, and an accommodative amplitude of 10 diopters. As both eyes accommodated equally and simultaneously converged, the subject fixated with the right eye at the reflection from a front surface mirror of an illuminated 20/50 near letter when it was at 25 cm from the cornea while the subject's left eye was video-graphed. The front surface mirror was adjusted to move the right eye so that the optic axis of the left eye was aligned with the central hole of the Placido

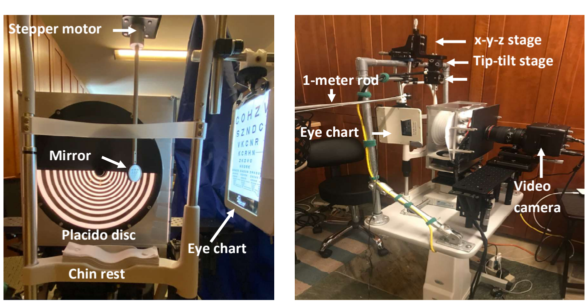

Figure 2. Setup for imaging the reflection of the semi-Placido disc rings from the posterior lens surface

978-1-6654-7029-2/22/$31.00©2022 IEEE IEEE SPMB 2022 December 3, 2022

disc through which the video images were obtained with a camera having a sensitivity better than 0.0005 lux, as shown in Figure 2.

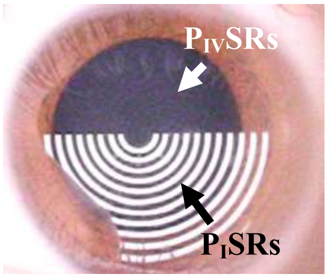

Figure 3. Barely visible posterior lens surface ($P_{IV}SRs$) and bright corneal (P_ISRs) reflections of the Placido disc semicircular rings.

Images of $P_{IV}SRs$ were dim [3] and noisy, as shown in Figure 3. A novel automated method is used to reduce the noise and find the $P_{IV}SRs$. As the first step of this method, temporal averaging was used to reduce noise. Because of micro-eye and head movements, shift-correction was performed to ensure image alignment prior to temporal averaging. To this end, the limbus (corneal-scleral transition) was detected. Using a one-time manual rectangle drawn on the nasal and also on the temporal limbus of a reference frame, the corresponding rectangles could be found in frames of other videos by cross-correlation. A temporal analysis window was chosen based on the smallest total of rectangle shifts. Frames in the window were spatially aligned and averaged. As eyelashes obscured portions of the image, they were manually identified and excluded from the analysis. Adaptive histogram equalization (AHE) [4] was used to increase the contrast between rings and the surrounding pixels, as shown in the first part of Figure 4.

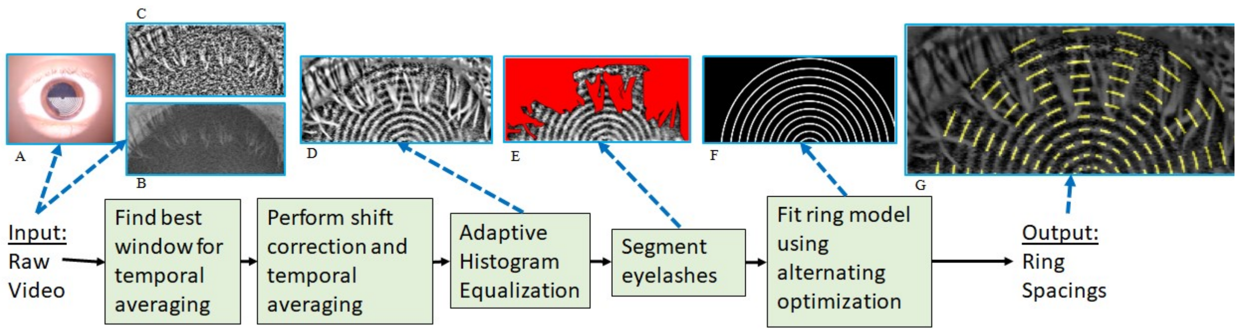

Figure 4. Image processing pipeline. A. Raw video; B. Close up of raw video in area of $P_{IV}SRs$; C. AHE version of $P_{IV}SRs$ shown only for purposes of visualization; D. $P_{IV}SRs$ after shift correction, temporal averaging, and AHE; E. Segmentation of eyelashes (red); F. Ring model fit using alternating optimization; G. Automated superposition of yellow model rings (dashes) on the temporally-averaged image

To find the locations of the $P_{IV}SRs$ in this enhanced image (EI), we modeled them as being composed of concentric elliptical rings. To ensure that all model rings have the same eccentricity, the minor to major axis ratio, $h=b_j/a_j$, was kept the same for all the model rings (j=1 to 11). The ring radii, $\{r_j\}$, were defined by:

$$r_j(\theta) = \frac{a_j b_j}{\sqrt{b_j^2 cos^2\theta + a_j^2 sin^2\theta}} \quad (1)$$

The model parameters were h, the common center of the ring coordinates (x_c, y_c), and the peak y coordinate p_j, which is related to the radius b_j for ring j at 90° by $p_j = b_j + y_c$. The model used a fixed intensity roll-off for the ring, where the intensity $I(x,y)$ at pixel (x,y) in the model image was a function of the distance from the ring along a meridian from the center. The model was then fit to the data in EI by alternating between two steps: *jointly* optimizing h, x_c, and y_c while holding $\{p_j\}$ fixed and then sequentially optimizing each peak p_j while holding h, x_c, and y_c and the other peaks fixed. In both steps, an objective function, the 2-D correlation coefficient between EI and the ring model, was evaluated at every point on a uniform grid. Iterative optimization was continued until convergence. The initial grid used empirically determined rough bounds for the parameters. Subsequent grids were centered on the best point of the previous grid with finer parameter bounds.

Table 1. Comparison of Automated and Manual Ring Placement Using the F-statistic Mean (η) and Standard Deviation (σ)

Video	1	2	3	4
# of Ring Pairs	21	21	20	21
η, Automated	148.9	150.5	201.4	152.5
σ, Automated	120.9	144.6	220.5	94.9
η, Manual	127.8	114.0	164.8	124.3
σ, Manual	108.0	119.0	190.1	87.2

For comparison to the automated method, the model elliptical rings were also manually aligned with the P_{IV}SRs. As will be seen, manual placement was less accurate and consistent than automated placement. Manual placement was difficult because of the interplay between the $\{p_j\}$, y_c, and h parameters. The placements were evaluated on shifted and temporally-averaged images without AHE by calculating an f-statistic between every adjacent pair of bright and dark rings (bright ring 1 and dark ring 1, dark ring 1 and bright ring 2, etc…), where *bright rings* were the previously-found rings in EI and *dark rings* were located in the spaces between these bright rings. Table 1 shows the f-statistic means and standard deviations over the ring pairs for manual and automated placement of the model rings in 4 separate videos of the subject focusing at the same distance. The consistently higher f-statistic values for automated placement demonstrate the success of the automated method. A paired one-sided t-test was evaluated on the 83 pairs of f-statistics; the resulting value of 0.0044 indicates a high probability that automated placement, illustrated for one video in Figure 4G, outperforms manual placement. Statistics for the spacing between a pair of rings along one meridian of the eye, obtained using the algorithm on the four videos, are shown in Table 2. Looking at the ratio of the standard deviation to the mean shows that automated placement produces more consistent estimates than manual placement.

To assess topographical changes of the posterior lens surface, the radius of curvature associated with each of the P_{IV}SRs can be calculated. Although precise equations are being derived in ongoing research, the general approach uses the standard mirror formulas [5]-[7], where $Magnification = -s'/s = -d'/d$, $1/s + 1/s' = -2/r$, r = radius of curvature, s = distance of the Placido disc from the posterior lens surface, s' = distance of P_{IV}SRs to the video camera, d = spacing between Placido disc rings, and d' = spacing between a corresponding pair of automatically placed rings. As d' (calculated via the algorithm), s, and d are known, r can be calculated from the mirror formulas. Although the optimization algorithm performs well visually and when compared to a human via the f-statistic, the variance is large compared to the topographical changes of the posterior lens surface. Consequently, in future research, reflections from the anterior lens surface, which are harder to detect [3], will be evaluated as its accommodative changes are significantly greater than those of the posterior surface [2]. Future research will also incorporate data from multiple patients, rather than a single patient, as person to person variability could impact success of the automated algorithm.

Table 2. Mean (η) and Standard Deviation (σ) of Ring Spacing (pixels) in 4 Videos

Ring Pair	1-2	2-3	3-4	4-5	5-6	6-7	7-8	8-9	9-10	10-11
η, Automated	8.08	8.50	8.28	8.38	8.65	8.70	9.20	9.54	9.88	10.30
σ, Automated	0.38	0.22	0.15	0.29	0.13	0.22	0.09	0.33	0.21	0.64
σ/ η (%) Automated	4.7	2.6	1.8	3.4	1.5	2.5	1.0	3.5	2.1	6.2
η, Manual	7.79	8.44	8.19	8.49	8.44	8.79	9.38	9.58	9.83	9.99
σ, Manual	0.11	0.53	0.15	0.26	0.14	0.35	0.47	0.27	0.43	1.27
σ/ η (%) Manual	1.4	6.3	1.8	3.1	1.7	3.9	5.0	2.9	4.3	13.7

In conclusion, our novel optical setup and processing pipeline with shift correction, temporal averaging, manual eyelash removal, and optimization of a concentric elliptical ring model visually and numerically fits the data well. Thus, this approach is suitable for calculating the posterior lens radius of curvature, revealing accommodative topographical changes of the lens surface and helping resolve whether the Helmholtz or Schachar theory is correct.

REFERENCES

[1]. H. von Helmholtz, "Uber die akkommodation des auges," *Archiv. Ophthalmol*, 1855, pp. 1:1–74.

[2]. R. Schachar, *The Mechanism of Accommodation and Presbyopia*, Amsterdam: Kugler Publications, 2012.

[3]. M. Suheimat, D. Bhattarai, H. Maher, M. Chandra, W. Chelepy, S. Halloran, A. Lambert, D. Atchison, "Improvements to phakometry using Bessel beams," *Optom Vis Sci*., 2017, vol. 94, pp. 1015-1021.

[4]. S. Pizer, E. Amburn, J. Austin, R. Cromartie, A. Geselowitz, T. Greer, B. Romeny, J. Zimmerman, and K. Zuiderveld, "Adaptive histogram equalization and its variations," *Computer Vision, Graphics, and Image Processing,* 1987, vol. 39, pp. 355-368.

[5]. F. Jenkins, H. White, *Fundamentals of Optics,* 3rd ed. New York: McGraw-Hill Book Co. 1957, pp. 509-512.

[6]. D. Mutti, K. Zadnik, A. Adams, "A video technique for phakometry of the human crystalline lens," *Invest Ophthalmol Vis Sci*., 1992, vol. 33, pp. 1771-82.

[7]. L. Garner, "Calculation of the radii of curvature of the crystalline lens surfaces," *Ophthalmic Physiol Opt.,* 1997, vol. 17, pp. 75-80.

Detecting Human Posterior Lens Surface Topographical Changes During Accommodation

E. Feldman[1], Y. Chen[2], R. Schachar[3] and P. Cosman[2]

1. Milken Community Schools, Los Angeles, California, USA

2. Department of Electrical and Computer Engineering, UC San Diego, San Diego, California, USA

3. Department of Physics, University of Texas at Arlington, Arlington Texas, USA

Abstract

Understanding accommodation is crucial to developing treatments for myopia, presbyopia, and glaucoma. A reflection of a placido disc off of the posterior lens surface of the eye is suitable for determining the topography of the posterior lens surface, once image enhancement and ring modeling are employed. Thus, these algorithmic steps, in conjunction with the optical setup proposed here, could be used to determine changes in topography, the key to understanding accommodation.

Introduction

- Accommodation, the eye's ability to focus up close by changing the shape of the lens, affects the development of myopia and glaucoma, and its age-related decline results in presbyopia
- Presbyopia affects 100% of the population in the fifth decade of life
- An understanding of accommodation is required to develop the best treatments for these maladies
- How the lens changes shape is still in dispute after more than 165 years. The fundamental issue is whether during accommodation the lens steepens centrally and peripherally (Helmholtz theory) or steepens centrally and peripherally flattens (Schachar theory)
- Magnetic resonance imaging (MRI), Schiempflug photography, and optical coherence tomography (OCT) all require curve fitting which reduces the detection accuracy of small changes of the peripheral lens surfaces, whose characterization is critical to understanding the accommodation mechanism

Figure 1: Lens Curvature Theories

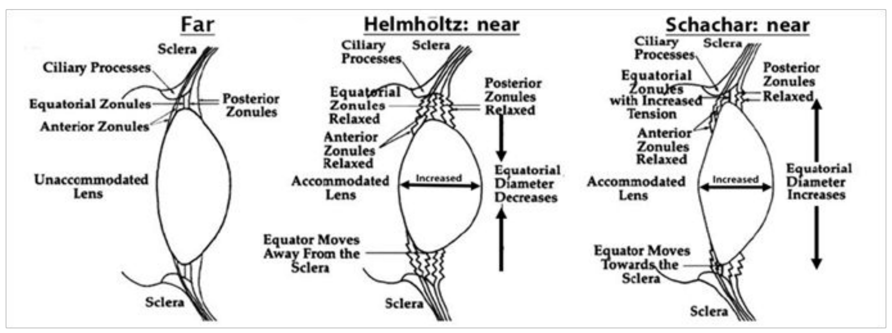

Methodology

- P_{IV}SRs, the reflection of a Placido disc (with 24 equally spaced rings, 12 illuminated and 12 black) off the posterior lens surface of eye, were collected from a single 20 year-old subject
- The subject fixated with the right eye on the reflection from a mirror of an illuminated 20/50 near letter chart when it was at 25 cm from the cornea while the subject's left eye was video-graphed
- The front surface mirror was adjusted to move the right eye so that the optic axis of the left eye was aligned with the central hole of the Placido disc through which the video images were obtained

Figure 2: Optical Setup

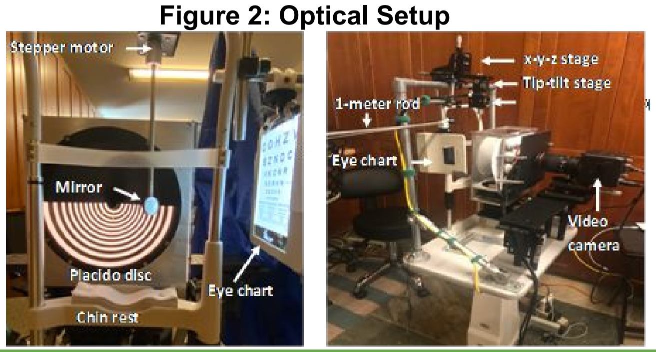

Figure 3: Algorithm Pipeline for Ring Modelling

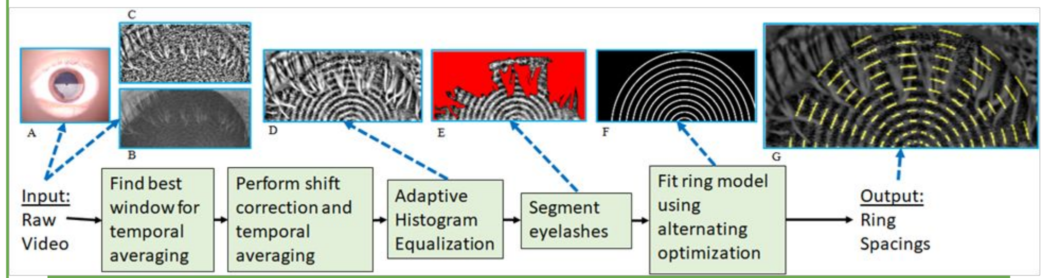

Image Enhancement

- Images of P_{IV}SRs were dim and noisy, so temporal averaging was used to reduce noise
- Because of micro-eye and head movements, shift-correction was performed to ensure image alignment prior to temporal averaging. To this end, the limbus (corneal-scleral transition) was detected on both sides of the eye in each frame using cross-correlation to manually-boxed limbus regions in a starting frame
- A temporal analysis window was chosen based on the smallest total of limbal shifts
- Frames in the window were spatially aligned and averaged
- Adaptive histogram equalization (AHE) was used to increase the contrast between rings and the surrounding pixels

Figure 4: Noisy P_{IV}SRs

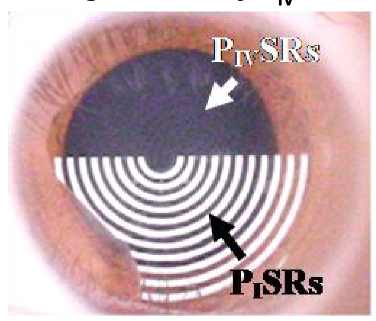

Ring Fitting

- To find the locations of the P_{IV}SRs in this enhanced image (EI), the P_{IV}SRs were modeled as concentric elliptical rings
- The minor to major axis ratio, $h=b_j/a_j$, was kept the same for all the model rings (j=1 to 11)
- The ring radii, $\{r_j\}$, were defined by:

$$r_j(\theta) = \frac{a_j b_j}{\sqrt{b_j^2 cos^2\theta + a_j^2 sin^2\theta}}$$

- The model parameters were h, the common center of the ring coordinates (x_c, y_c), and the peak y coordinate p_j, which is related to the radius b_j for ring j at 90° by $p_j = b_j + y_c$
- The model used a fixed intensity roll-off for the ring, where the intensity $I(x,y)$ at pixel (x,y) in the model image was a function of the distance from the ring along a meridian from the center
- The model was then fit to the data in EI by alternating between two steps: *jointly* optimizing h, x_c, and y_c while holding $\{p_j\}$ fixed and then sequentially optimizing each peak p_j while holding h, x_c, and y_c and the other peaks fixed
- In both steps, an objective function, the 2-D correlation coefficient between EI and the ring model, was evaluated at every point on a uniform grid
- Iterative optimization was continued until convergence.
- The initial grid used empirically-determined rough bounds for the parameters
- Subsequent grids were centered on the best point of the previous grid with finer parameter bounds

Statistical Analysis

- The placements were evaluated on shifted and temporally-averaged images without AHE by calculating an f-statistic between every adjacent pair of bright and dark rings (bright ring 1 and dark ring 1, dark ring 1 and bright ring 2, etc…), where the *bright rings* were the previously-found rings in EI and *dark rings* were located in the spaces between these bright rings
- The consistently higher f-statistic values for automated placement, as seen in Table 1, demonstrate the success of the automated method
- A paired one-sided t-test was evaluated on the 83 pairs of f-statistics; the resulting value of 0.0044 indicates a high probability that automated placement outperforms manual placement
- Statistics for the spacing between a pair of rings along one meridian of the eye, obtained using the algorithm on the four videos, are shown in Table 2
- Looking at the ratio of the standard deviation to the mean shows that automated placement produces more consistent estimates than manual placement

Table 1: F-statistic Values for Automated and Manual Placement

Video	1	2	3	4
# of Ring Pairs	21	21	20	21
η, Automated	148.9	150.5	201.4	152.5
σ, Automated	120.9	144.6	220.5	94.9
η, Manual	127.8	114.0	164.8	124.3
σ, Manual	108.0	119.0	190.1	87.2

Table 2: Consistency of Ring Placements

Ring Pair	1-2	2-3	3-4	4-5	5-6	6-7	7-8	8-9	9-10	10-11
η, Automated	8.08	8.50	8.28	8.38	8.65	8.70	9.20	9.54	9.88	10.30
σ, Automated	0.38	0.22	0.15	0.29	0.13	0.22	0.09	0.33	0.21	0.64
σ/ η (%) Automated	4.7	2.6	1.8	3.4	1.5	2.5	1.0	3.5	2.1	6.2
η, Manual	7.79	8.44	8.19	8.49	8.44	8.79	9.38	9.58	9.83	9.99
σ, Manual	0.11	0.53	0.15	0.26	0.14	0.35	0.47	0.27	0.43	1.27
σ/ η (%) Manual	1.4	6.3	1.8	3.1	1.7	3.9	5.0	2.9	4.3	13.7

Conclusions

To assess topographical changes of the posterior lens surface, the radius of curvature associated with each of the P_{IV}SRs can be calculated. Although precise equations are being derived in ongoing research, the general approach uses the standard mirror formulas. Our novel optical setup and processing pipeline with shift correction, temporal averaging, and optimization of a concentric elliptical ring model visually and numerically fits the data well. Thus, this approach is suitable for calculating the posterior lens radius of curvature, revealing accommodative topographical changes of the lens surface and helping resolve whether the Helmholtz or Schachar theory is correct. Although the optimization algorithm performs well visually and when compared to a human via the f-statistic, the variance is large compared to the topographical changes of the posterior lens surface and requires refinement to provide the necessary precision.

Next Steps

In future research, reflections from the anterior lens surface, which are harder to detect, will be evaluated as its accommodative changes are significantly greater than those of the posterior surface. Future research will also incorporate data from multiple patients, rather than a single patient, as person to person variability could impact success of the automated algorithm.